Eur. Phys. J. A **12**, 487–493 (2001)

THE EUROPEAN PHYSICAL JOURNAL A

Incoherent X-radiation produced by relativistic electrons in crystals

V.B. Gavrikov[1,a], V.P. Likhachev[2], J.D.T. Arruda-Neto[2,3], and A.L. Bonini[2]

[1] Kharkov Institute of Physics and Technology, 1 Akademishna 61108 Kharkov, Ukraine
[2] Laboratório do Acelerador Linear, Instituto de Física da Universidade de São Paulo, CP66318, 05315-970 São Paulo, SP, Brazil
[3] University of Santo Amaro/UNISA, Brazil

Received: 2 July 2001 / Revised version: 29 September 2001
Communicated by Th. Walcher

Abstract. Differential and integral features of incoherent X-radiation, induced by relativistic electrons in crystals, are studied for observation angles θ_γ several times greater than γ^{-1}, where γ is the projectile Lorentz factor. The existence of sharp maxima and a minimum of the five-folded incoherent differential cross-section as a function of the final electron angles, and a dip minimum when the cross-section is taken as a function of the photon energies, is demonstrated. At near backward observation angles the three-folded cross-section shows a maximum in the region of several keV photon energies. The obtained results allow us to optimize the conditions for coincidence experiments, minimizing the incoherent contribution to the total radiation yield, and helping to analyse results of finite-size detector experiments with crystal targets.

PACS. 41.75.Ht Relativistic electron and positron beams – 78.70.Ck X-ray scattering

1 Introduction

The passage of a relativistic charged particle through a crystalline target is accompanied by the emission of coherent and incoherent radiation. The properties of coherent X-radiation produced by electrons of several tens of MeV in a crystalline target, like absolute intensity [1,2] spectral and angular dependences [2–4] and interference effect [5, 6] have been thoroughly investigated. The results of those studies were summarized in [4], where it was shown quantitatively that quasi-monochromatic, tunable and polarized X-radiation sources, using moderate electron beam energies, can be designed based on the coherent X-radiation process. Such sources might be used for purposes of medical physics, industrial radiography and in a variety of other areas.

The properties of the incoherent bremsstrahlung were studied only in earlier works [7,8] without taking into account the radiation from crystal electrons. Thus, the problem was restricted to the case where the projectiles radiate in screened fields of crystal nuclei and in the near-forward direction. At the same time, at large observation angles the radiation from the target is formed mainly by the polarization mechanism and, to our knowledge, this question is not investigated yet.

The aim of the present paper is to study the differential and integral properties of incoherent X-ray bremsstrahlung produced in a crystal by a relativistic electron with several tens of MeV and observed at angles θ_γ several times greater than γ^{-1}, where γ is the projectile Lorentz factor, *i.e.*, for those observation angles, where the contribution of the polarization term to the total cross-section is comparable with the static one or dominates the whole process. We carry out our study for the case when a projectile interacts with a crystal atom as a whole. As a result, the interference effect between different radiation mechanisms could be important.

A detailed knowledge of the differential cross-section, as well as the cross-section integrated over the angles of the final electron, are of particular importance for the analysis of experiments using finite-size detectors. An evaluation of the cross-section for a particular set of angles could give totally incorrect values for the cross-section integrated over the finite detector solid angles, as shown by Maximon *et al.* [9]. In this respect, we point out the results obtained in [10], where it was found that the absolute intensity of the parametric X-radiation, detected near 180° with respect to the direction of the electron beam and at photon energies of ~ 3 keV, is twice larger as predicted from the kinematic theory. As shown in the present paper, at such photon energies and observation angles, the incoherent cross-section achieves its maximum and,

[a] e-mail: gravrikov@axpfep1.if.usp.br

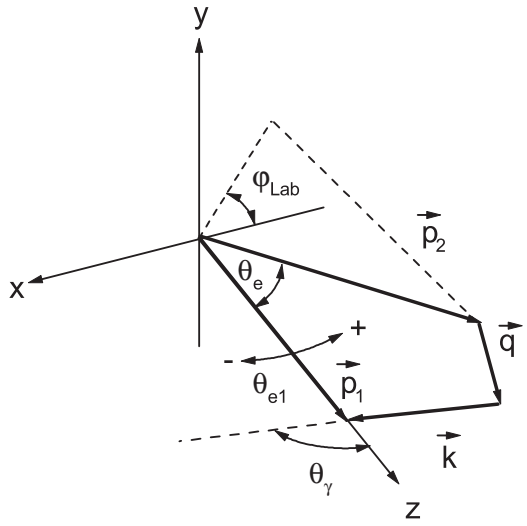

Fig. 1. The laboratory coordinate system. $\mathbf{k}$ is the wave vector of the bremsstrahlung photon; $\mathbf{p}_1$ and $\mathbf{p}_2$ are the initial and final momenta of the incident electron, respectively. $\mathbf{p}_1$ is directed along the z-axis, θ_γ is the angle between $\mathbf{k}$ and $\mathbf{p}_1$; θ_e is the angle between $\mathbf{p}_1$ and $\mathbf{p}_2$; $\theta_{\mathrm{e}1}$ is the angle between $\mathbf{p}_1$ and $\mathbf{p}_2$, when $\mathbf{p}_2$ lies in the (x, z)-plane; φ_Lab is the angle between the planes $(\mathbf{k}, \mathbf{p}_1)$ and $(\mathbf{p}_1, \mathbf{p}_2)$.

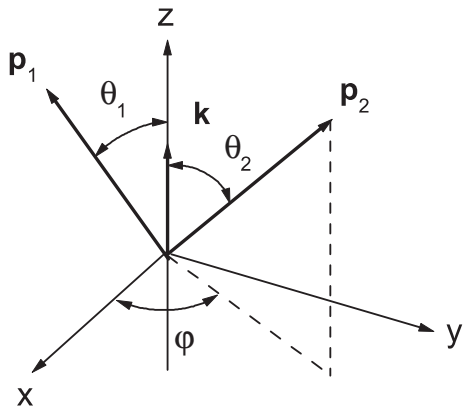

Fig. 2. The photon-oriented coordinate system. φ is the angle between the planes $(\mathbf{k}, \mathbf{p}_1)$ and $(\mathbf{k}, \mathbf{p}_2)$.

therefore, the above experimental result could be explained as a contribution of incoherent radiation components to the resulting radiation yield.

2 Incoherent cross-section

2.1 General notation

The momentum diagram of the considered process is shown in fig. 1. The initial electron with momentum $\mathbf{p}_1$ and energy E_1 interacts with a crystalline target and, in the final state, there are a scattered electron with momentum $\mathbf{p}_2$, energy E_2 and a bremsstrahlung photon with momentum $\mathbf{k}$ and energy ω. During this interaction the target acquires momentum $\mathbf{q} = \mathbf{p}_1 - \mathbf{p}_2 - \mathbf{k}$. The q-range spans from q_min up to q_max. Both q_min and q_max are defined by the energy and momentum conservation laws.

We will examine the low momentum transfer region, where the projectile interacts with an atom as a whole, and the long-wavelength approximation is valid. The radiation matrix element is a sum of two terms, where the first corresponds to static (Bethe-Heitler) bremsstrahlung, emitted by the projectile itself, and the second arises from the dynamic polarization of the atomic electrons in the fields of the incoming particle and the bremsstrahlung photon ("atomic" bremsstrahlung [11],[12]). To avoid cancellations and losses of sharp structure effects in the five-folded differential cross-section, the study of the differential properties of the cross-section and its integration over the solid angle for the outgoing electrons are most convenient to accomplish in the photon-oriented coordinate system (fig. 2), a spherical coordinate system where the polar axis coincides with the photon momentum direction. In this system, the angles θ_1 and θ_2 describe the initial and final electron momentum directions. In the following analysis, we will use the photon and laboratory systems, but the final results will be presented in the laboratory system, where the z-axis is directed along the vector $\mathbf{p}_1$. In this system, θ_γ is the angle between the vectors $\mathbf{k}$ and $\mathbf{p}_1$, $\theta_\gamma = \theta_1$, and θ_e is the angle between $\mathbf{p}_1$ and $\mathbf{p}_2$, as shown in fig. 1.

2.2 The crystal cross-section

The radiation cross-section, in the case of a crystal, can be written for photon energies greater than the electronic binding energies as a product of the diffraction factor f and an atomic cross-section $\mathrm{d}\sigma_\mathrm{at}$, in the following way [7, 8]:

$$\mathrm{d}\sigma_\mathrm{cr} = f\mathrm{d}\sigma_\mathrm{at} = \mathrm{d}\sigma_\mathrm{inc} + \mathrm{d}\sigma_\mathrm{coh}, \tag{1}$$

and f is the sum of the incoherent and coherent parts,

$$f = f_\mathrm{inc} + f_\mathrm{coh}, \tag{2}$$

and

$$f_\mathrm{inc} = \left[1 - \exp\left(-q^2u^2\right)\right],$$
$$f_\mathrm{coh} = \frac{(2\pi)^3}{V_\mathrm{c}N}\exp\left(-q^2u^2\right)\sum_{\mathbf{g}} S^2\left(\mathbf{q}\right)\delta\left(\mathbf{q}-\mathbf{g}\right).$$

In eq. (2) u^2 is the mean-square temperature displacement of the atoms from their equilibrium positions; V_c is the volume of the unit crystal cell; $\mathbf{g}$ is a reciprocal lattice vector; N is the number of atoms per unit cell; and $S\left(\mathbf{q}\right)$ is the crystal structure factor, $S\left(\mathbf{q}\right) = \sum \exp(i\mathbf{q}\mathbf{r}_i)$, where $\mathbf{r}_i$ describes the position of the i-th atom within the cell. Note that both the incoherent and coherent cross-sections are normalized for a target thickness of 1 atom/cm^2.

As it follows from eq. (1), the coherent cross-section $\mathrm{d}\sigma_\mathrm{coh}$ can be large only when the momentum transferred is very close to that of the reciprocal lattice vectors. In this case, each atom in the crystal gives a contribution

to the radiative matrix element and, therefore, the coherent X-radiation can be considered as a process involving only two particles, namely, the relativistic electron and the crystal. In contrast with the coherent process, the momentum transfer spectrum for the incoherent process is a continuum. The crystal atoms make their contributions to the incoherent radiative amplitude with different phases, and the cross-section of radiation generated by the interaction between the projectile and a single atom in the crystal is multiplied by the incoherent factor $f_{\rm inc}$, which can be significantly smaller than 1, as compared to the amorphous case.

2.3 The atomic cross-section

The amplitude of the radiation due to the interaction of the projectile with the screened nucleus is well known [13], and for our purposes it can be presented in the form ($\hbar = c = 1$):

$$M_{\rm st} = \frac{(2\pi)^{3/2} e^3}{m(E_1 E_2 \omega)^{1/2}} \frac{Z - F(q)}{\gamma q^2} \mathbf{e}_f \left[\frac{\mathbf{p}_1}{\omega - \mathbf{k}\mathbf{v}_1} - \frac{\mathbf{p}_2}{\omega - \mathbf{k}\mathbf{v}_2} \right], \tag{3}$$

where $\mathbf{e}_f$ is the polarization vector of the photon; e and m are the electron charge and mass, respectively; Z is the atomic number of the crystal; $\mathbf{v}_1$ and $\mathbf{v}_2$ are the projectile velocities before and after radiation, respectively, and $F(q)$ is the form factor of the atom. The general expression for the polarization amplitude, in the case of the non-relativistic atom, has been obtained by Amusia *et al.* [14]:

$$M_{\rm pol} = \frac{(2\pi)^{3/2} e}{(E_1 E_2 \omega)^{1/2}} \mathbf{e}_f \frac{\omega \mathbf{v}_1 - \mathbf{q}}{(\mathbf{k} + \mathbf{q}) - k^2} \omega \alpha(\omega, q), \tag{4}$$

where $\alpha(\omega, q)$ is the dynamic polarizability of the atom. Note that, process described by $M_{\rm pol}$ is equivalent to the coherent Rayleigh scattering of virtual photons associated with the projectile. For the photon energies under consideration, the function $\alpha(\omega, q)$ can be replaced by $-e^2 F(q)/m\omega^2$, and the total radiation cross-section summed over photon polarizations has the form [15]:

$$\mathrm{d}\sigma_{\rm at} = \sigma_0(\omega) Z^2 p_2^2 \mathrm{d}\omega \mathrm{d}\Omega_\gamma \mathrm{d}\Omega_{p_2} \times \left[\mathbf{n} \times \left(\frac{1 - F(q)}{\gamma q^2 (1 - \beta \cos\theta_\gamma)} \mathbf{q} + \frac{F(q)}{(\mathbf{k}+\mathbf{q}) - k^2} (k\beta - \mathbf{q}) \right) \right]^2. \tag{5}$$

In eq. (5) $\sigma_0(\omega) = \alpha r_{\rm e}^2/\pi^2\omega$; α=1/137; $r_{\rm e}$ is the classical electron radius; $\beta \equiv \mathbf{v}_1$; $\mathbf{n} = \mathbf{k}/k$; $\mathrm{d}\Omega_{p_2}$ is a solid angle around the direction of $\mathbf{p}_2$ and $\mathrm{d}\Omega_\gamma$ is a solid angle around θ_γ.

In the photon-oriented coordinate system (fig. 2), the atomic cross-section, eq. (5), can be presented in the following form:

$$\mathrm{d}\sigma_{\rm at} = \mathrm{d}\sigma_{\rm st} + \mathrm{d}\sigma_{\rm pol} + \mathrm{d}\sigma_{\rm int}, \tag{6}$$

where

$$\mathrm{d}\sigma_{\rm st} = \sigma_0(\omega) Z^2 p_2^2 \left[\frac{1 - F(q)}{\gamma q^2 (1 - \beta \cos\theta_\gamma)} \right]^2 T_1 \mathrm{d}\omega \mathrm{d}\Omega_\gamma \mathrm{d}\Omega_{p_2}, \tag{7}$$

$$\mathrm{d}\sigma_{\rm pol} = \sigma_0(\omega) Z^2 p_2^2 F^2(q)\, T_2 \mathrm{d}\omega \mathrm{d}\Omega_\gamma \mathrm{d}\Omega_{p_2},$$

$$\mathrm{d}\sigma_{\rm int} = \sigma_0(\omega) Z^2 p_2^2 \frac{2F(q)\,[1 - F(q)]}{\gamma q^2 (1 - \beta \cos\theta_\gamma)} T_3 \mathrm{d}\omega \mathrm{d}\Omega_\gamma \mathrm{d}\Omega_{p_2},$$

$$T_1 = p_1^2 \sin^2\theta_\gamma + p_2^2 \sin^2\theta_2 - 2p_1 p_2 \sin\theta_\gamma \sin\theta_2 \cos\varphi,$$

$$T_2 = \frac{k^2\beta^2 \sin^2\theta_\gamma - 2k\beta \sin\theta_\gamma [p_1 \sin\theta_\gamma - p_2 \sin\theta_2 \cos\varphi] + T_1}{\left[2k\,(p_1 \cos\theta_\gamma - p_2 \cos\theta_2 - k) + q^2\right]^2},$$

$$T_3 = \frac{k\beta \sin\theta_\gamma\,[p_1 \sin\theta_\gamma - p_2 \sin\theta_2 \cos\varphi] - T_1}{2k\,(p_1 \cos\theta_\gamma - p_2 \cos\theta_2 - k) + q^2},$$

$$q = p_1^2 + p_2^2 + k^2 - 2p_1 k \cos\theta_\gamma + 2p_2 k \cos\theta_2 - 2p_1 p_2\,(\cos\theta_\gamma \cos\theta_2 + \sin\theta_\gamma \sin\theta_2 \cos\varphi)$$

and φ is the angle between the planes $(\mathbf{k}, \mathbf{p}_1)$ and $(\mathbf{k}, \mathbf{p}_2)$ as in fig. 2. In eq. (6) $\mathrm{d}\sigma_{\rm st}$ and $\mathrm{d}\sigma_{\rm pol}$ represent the static and polarization contributions, respectively, and $\mathrm{d}\sigma_{\rm int}$ describes the contribution resulting from the interference effect between these processes. Note that the connection between φ and $\varphi_{\rm Lab}$, which is the angle between the planes $(\mathbf{k}, \mathbf{p}_1)$ and $(\mathbf{p}_1, \mathbf{p}_2)$ in the laboratory system, is

$$\tan\varphi = \frac{\sin\theta_{\rm e} \sin\varphi_{\rm Lab}}{\sin\theta_{\rm e} \cos\varphi_{\rm Lab} \cos\theta_\gamma + \cos\theta_{\rm e} \sin\theta_\gamma}. \tag{8}$$

The incoherent radiation cross-section is the product of the atomic cross-section, eq. (6), and $f_{\rm inc}$, eq. (2).

3 Results and discussion

3.1 Properties of $\mathrm{d}^5\sigma_{\rm inc}/\mathrm{d}\omega\mathrm{d}\Omega_\gamma\mathrm{d}\Omega_{p2}$

The main differential characteristics of the incoherent cross-section are presented in figs. 3-7. We next consider the case of a silicon crystal which is kept at the room temperature.

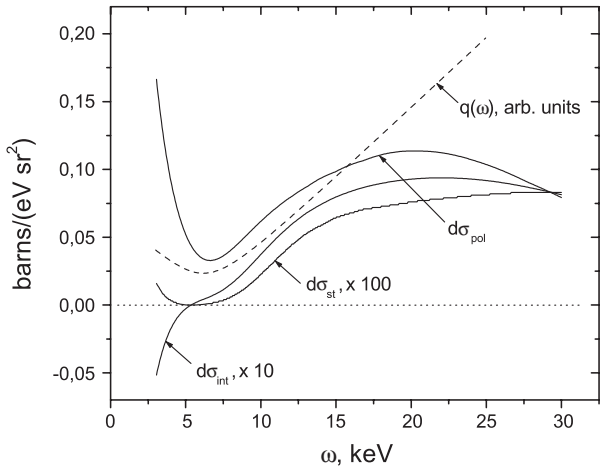

Fig. 3. Contributions to the incoherent five-folded cross-section. $\mathrm{d}\sigma_{\rm st}$, $\mathrm{d}\sigma_{\rm int}$, and $\mathrm{d}\sigma_{\rm pol}$ in a silicon crystal are shown as functions of ω. $E_1 = 15$ MeV, $\theta_\gamma = 40^\circ, \theta_{\rm e} = 3 \times 10^{-4}$ rad, $\varphi_{\rm Lab} = 0^\circ$. The function $q(\omega)$ is represented by the dashed line.

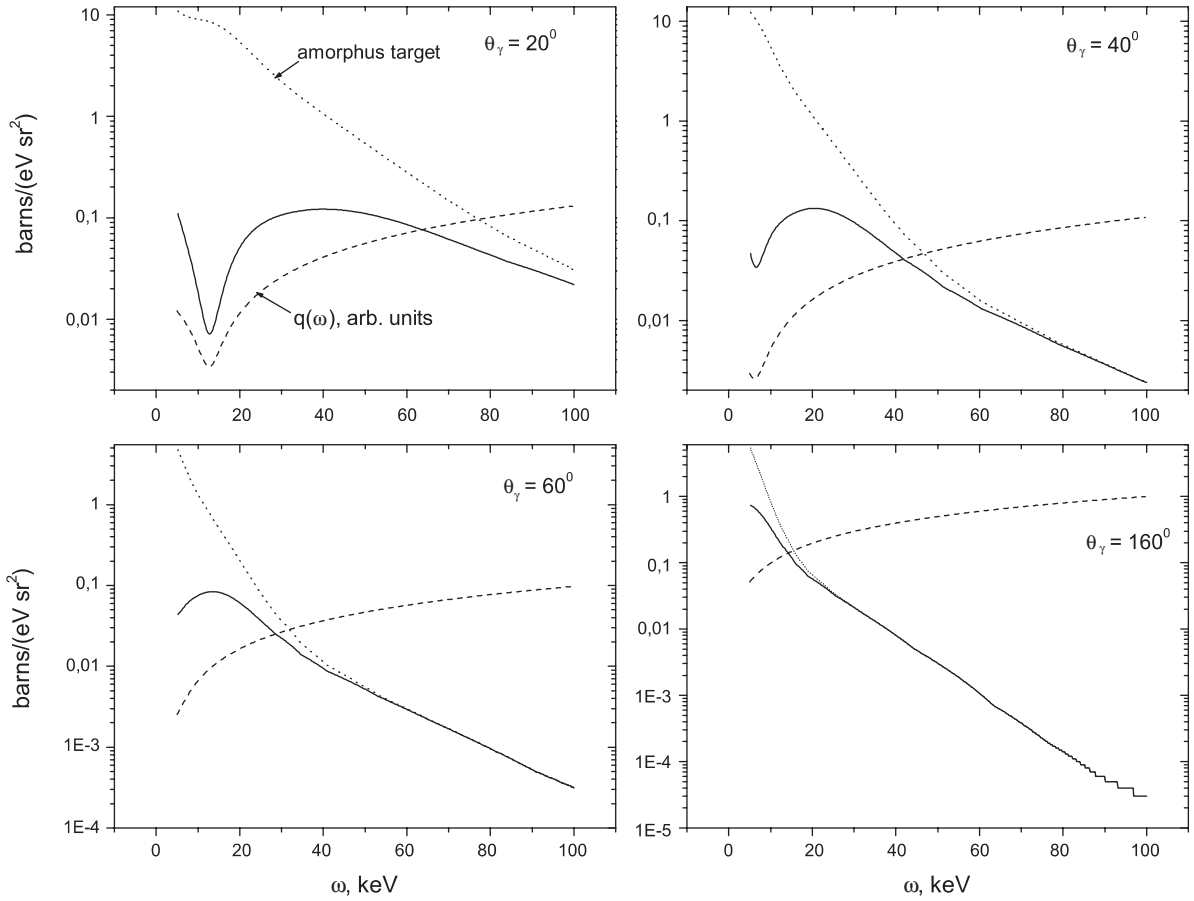

Fig. 4. Total five-folded incoherent cross-section as a function of the photon energy for $\theta_e = 3 \times 10^{-4}$ rad, $E_1 = 15$ MeV, $\varphi_{Lab} = 0^\circ$ and four selected values of θ_γ. The dotted lines denote dependences for the amorphous case, and the dashed lines are for $q(\omega)$.

The dependence of the five-folded incoherent cross-section components, $d\sigma_{st}$, $d\sigma_{int}$, and $d\sigma_{pol}$ on the photon energy is shown in fig. 3 for $\theta_\gamma = 40^\circ$ and for those angles in the photon-oriented system, which correspond to the laboratory system angles $\theta_e = 3 \times 10^{-4}$ rad and $\varphi_{Lab} = 0$. The dashed line in this figure indicates the dependence $q(\omega)$. It is clear that the main contributions to the total five-folded incoherent cross-section come from $d\sigma_{pol}$ and $d\sigma_{int}$. The cross-sections $d\sigma_{st}$ and $d\sigma_{pol}$ have minima at photon energies corresponding to momentum transfers close to the kinematically allowed minimum, $q \backsim q_{min}$, where

$$q_{min} = k(1-\cos\theta_\gamma) + \frac{1}{2}\frac{k^2}{p_1}(1+\sin^2\theta_\gamma) + O(k^3/p_1^2). \quad (9)$$

As shown in fig. 3, the interference contribution changes its sign at $q = q_{min}$. Note that in the case of relativistic positrons $d\sigma_{int}$ has the opposite sign.

In fig. 4 the dependence of the total five-folded incoherent cross-section *versus* photon energy is shown for $\theta_e = 3 \times 10^{-4}$ rad, $\varphi_{Lab} = 0^\circ$ and for four observation angles. In these figures the functions $q(\omega)$ are represented by the dashed lines, and the dotted lines show the corresponding dependences for the case of an amorphous target. As it follows from the figures, the dependences of the cross-sections in the crystal and amorphous cases differ strongly for all observation angles exept θ_γ near the backward direction.

Introducing the vector $\Delta\mathbf{p} = \mathbf{p}_1 - \mathbf{p}_2 = \mathbf{q} + \mathbf{k} = \Delta\mathbf{p}_\perp + \Delta\mathbf{p}_\parallel$, where $|\Delta\mathbf{p}_\perp| = p_2\theta_e$, $|\Delta\mathbf{p}_\parallel| = p_1 - p_2$ we can write in the laboratory system $q^2 = (\Delta p_\parallel - k\cos\theta_\gamma)^2 + \Delta p_\perp^2 \cos^2\varphi_{Lab} + (\Delta p_\perp \sin\varphi_{Lab} - k\sin\theta_\gamma)^2$ and find that q^2 achieves its minimal value at

$$\omega_{min} = \frac{bp_1\theta_e(\cos\varphi_{Lab}(\theta_e\cos\varphi_{Lab} + b\sin\theta_\gamma) + \theta_e\sin\varphi_{Lab})}{(1-b\cos\theta_\gamma)^2 + (\theta_e\cos\varphi_{Lab} + b\sin\theta_\gamma)^2 + \theta_e^2\sin^2\varphi_{Lab}}, \quad (10)$$

where $b = p_1/E_1$. The incoherent cross-section minimum shifts to higher photon energies as θ_e increases, and it shifts to the extremely soft energy range as the observation angle increases. At fixed θ_e minima in $q(\omega)$ and, therefore, in the cross-section, disappear at angles $\varphi_{Lab} \geqslant |\pi + \Delta\varphi|$, where

$$\Delta\varphi = \frac{\theta_e}{b\sin\theta_\gamma} \quad (11)$$

and at $\varphi_{Lab} = 0$ they disappear for observation angles larger than $\theta_{\gamma 0}$, where $\theta_{\gamma 0} = \pi - \theta_e/2$.

The angular dependence of the partial cross-section components on θ_{e1}, where θ_{e1} is the angle between $\mathbf{p}_1$ and

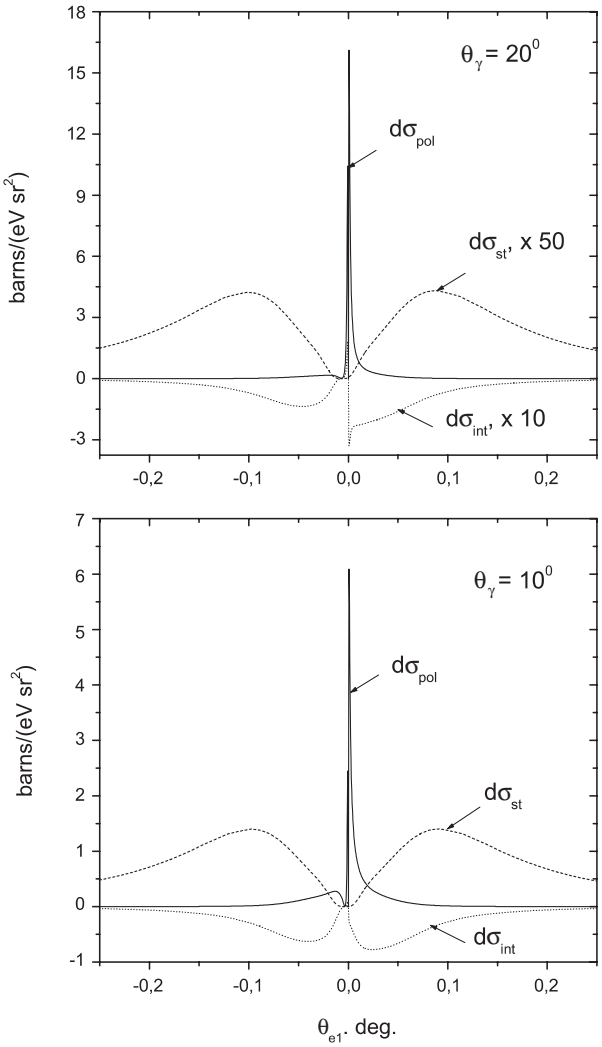

Fig. 5. The contributions of various mechanisms to the five-folded incoherent cross-section as functions of $\theta_{\rm e1}$ (see fig. 1) for $E_1 = 15$ MeV, $\omega = 5$ keV and pointed out θ_γ.

$\mathbf{p}_2$, when $\mathbf{p}_2$ lies in the (x, z)-plane (fig. 1), is shown in fig. 5 for the cases $\theta_\gamma = 10°, 20°$ and $\omega = 5$ keV. The cross-sections vary with $\theta_{\rm e1}$ rapidly and $\mathrm{d}\sigma_{\rm pol}$ makes its contribution to the total cross-section into much narrow angle range than $\mathrm{d}\sigma_{\rm st}$. As the observation angle increases, the static and interference contributions become negligible.

For the cases $\theta_\gamma = 40°$ ($\omega = 5$ and 30 keV) and $\theta_\gamma = 160°$ ($\omega = 5$ keV) the angular dependence of the cross-section on $\theta_{\rm e1}$ is shown in fig. 6. It is seen from this figure that, for the observation angles we pointed out, the cross-section has a "two-hump" character. To find values of $\theta_{\rm e1}$, at which the cross-section achieves its extrema, we note that at large θ_γ the main contribution to the cross-section arises from the polarization term and, therefore, the incoherent cross-section is proportional to the square of the function

$$f(\theta_\gamma, \theta_{\rm e1}, k) = \frac{(k\beta - \Delta p_\parallel)\sin\theta_\gamma - \Delta p_\perp \cos\theta_\gamma}{\Delta p^2 - k^2}. \quad (12)$$

The extrema are then determined from $\partial f/\partial\theta_{\rm e1} = 0$, from which it can be found that the maximal values of the cross-section are at angles

$$\theta_{e1,\max} = \pm\frac{1}{p_1}\sqrt{\Delta p_\parallel^2 - k^2}, \quad (13)$$

and $\mathrm{d}^5\sigma_{\rm inc}$ achieves its minimun at

$$\theta_{e1,\min} = -\frac{k}{2\gamma^2 p_1}\tan\theta_\gamma + O(k^2/p_1^2). \quad (14)$$

As follows from eq. (13), the position of maximal cross-section values do not depend on θ_γ. The angular dependence of the cross-section changes drastically as θ_γ achieves values near to 90°. This fact is illustrated by fig. 7, where the cross section is shown for $\theta_\gamma = 85°$ and 90°. At $\theta_\gamma = 90°$ the cross-section has only one maximum localized at $\theta_{\rm e1} = 0°$.

By using eq. (12) we can find the ratio between the cross-section maxima. Noting that $F(q)$ as well as the incoherent diffraction factor differ very small at points given

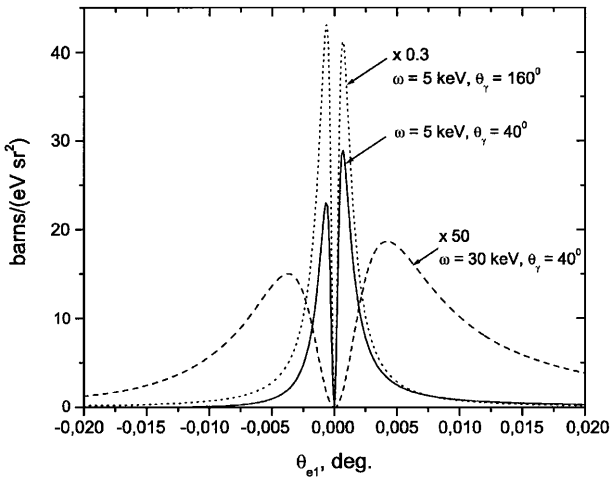

Fig. 6. The five-folded cross-sections as functions of $\theta_{\rm e1}$ (see fig. 1) for $E_1 = 15$ MeV and selected sets of ω and θ_γ.

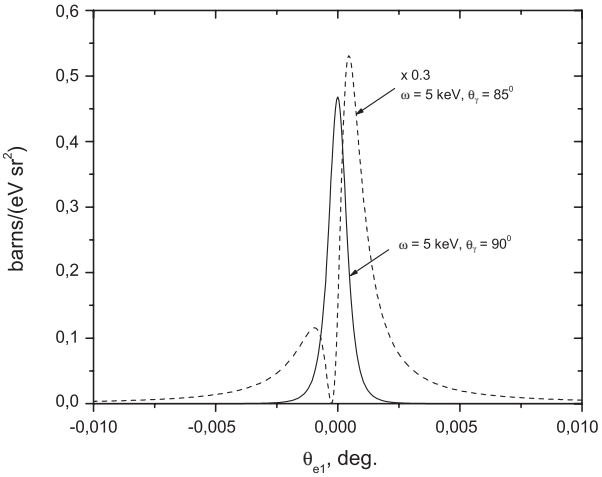

Fig. 7. The five-folded cross-sections at $\theta_\gamma = 85°$ and 90°, $E_1 = 15$ MeV.

by eq. (13), it can be found that

$$\frac{\mathrm{d}^5\sigma_{\mathrm{inc}}^{(-)}}{\mathrm{d}^5\sigma_{\mathrm{inc}}^{(+)}} = \left[\frac{(k\beta - \Delta p_{\parallel})\sin\theta_\gamma - p_2\,|\theta_{e1,\max}|\cos\theta_\gamma}{(k\beta - \Delta p_{\parallel})\sin\theta_\gamma + p_2\,|\theta_{e1,\max}|\cos\theta_\gamma}\right]^2, \tag{15}$$

where the indexes $(-), (+)$ refer to the sign of θ_{e1} (fig. 1).

We observe from eq. (15) that the relation between the cross-section maxima changes when the observation angle becomes higher than 90°. This fact is illustrated in fig. 6 for $\theta_\gamma = 40°$ and 160°.

3.2 Properties of $\mathrm{d}^3\sigma_{\mathrm{inc}}/\mathrm{d}\omega\mathrm{d}\Omega_\gamma$

As it seems from the above consideration, the five-folded cross-section has a complex character with dip minima and maxima, and considerable care is required for the integration of the five-folded cross-section over the final electron angles. We integrated $\mathrm{d}^5\sigma_{\mathrm{inc}}$ in the photon-oriented coordinate system using the Monte Carlo approach [16]. The upper limit for momentum transfers was defined as $q \leqslant 5a^{-1}$, where $a = 0.885a_0Z^{-1/3}$ is a screening (Thomas-Fermi) radius with a_0 the Bohr radius. At integration, the values of $F(q)$ were obtained by linear interpolation from the values given in [17]. The integration in the region $q > 5a^{-1}$ gives only a few percent contribution to the final result. The angle φ was generated randomly in the range $\pm\varphi_{\max}$ with uniform distribution. The angle θ_2 was generated randomly in the range $[\theta_{\min}, \theta_{\max}]$ with the distribution uniform in $\cos\theta_2$:

$$\theta_2 = \arccos\left(\cos\theta_{\min} - (\cos\theta_{\min} - \cos\theta_{\max})\,\xi\right),$$

where ξ is a chance number uniformily distributed in the range $[0, 1]$; $\theta_{\min}$, $\theta_{\max}$ and $\varphi_{\max}$ are the angular limits in the photon-oriented system corresponding to $q = 5a^{-1}$. The relations between these angles and laboratory system angles can be found in [16].

The set of the three generated angles θ_1, θ_2 and φ was used for the calculation of q, and if q were less than $q_{\max}$ this set would be used to calculate the average five-folded differential cross-section:

$$\left\langle \mathrm{d}^5\sigma \right\rangle = \frac{1}{N}\sum_{i=1}^{N}\mathrm{d}^5\sigma_{\mathrm{i}},$$
$$\mathrm{d}^3\sigma = \left\langle \mathrm{d}^5\sigma \right\rangle \Delta\Omega,$$

where N is the number of the Monte Carlo starts, and $\Delta\Omega$ is the secondary electron solid angle, which was also calculated by MC simulation in the photon-oriented system [16].

The contributions of the various mechanisms to the three-folded incoherent cross-section, as functions of the observation angle, are presented in fig. 8 for an electron beam energy of 15 MeV. It is seen from this figure that the polarization contribution begins to play an essential role in the total radiation yield at $\theta_\gamma \gtrsim 20°$. The most prominent feature of the incoherent cross-section in a crystal is the maximum near the backward observation direction.

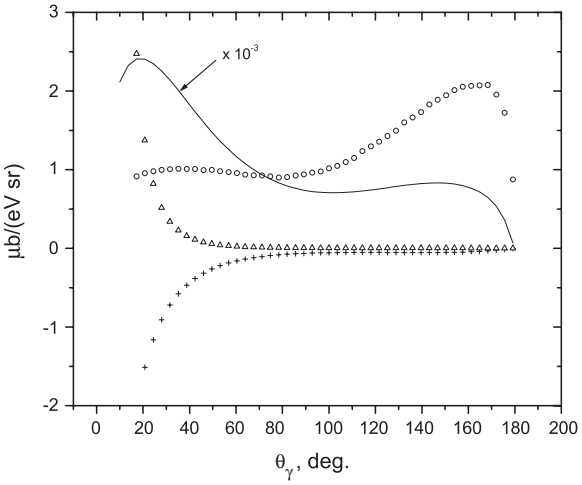

Fig. 8. The contributions of various mechanisms to the three-folded incoherent cross-section in a silicon crystal as functions of θ_γ for $E_1 = 15$ MeV and $\omega = 5$ keV. The open circles correspond to $\mathrm{d}^3\sigma_{\mathrm{pol}}$, crosses to $\mathrm{d}^3\sigma_{\mathrm{int}}$ and triangles to $\mathrm{d}^3\sigma_{\mathrm{st}}$. The solid curve shows the polarization contribution for a non-crystal target.

This maximum results from the decreasing of the denominator in eqs. (4) at these conditions. Note that the above feature results from the suppression of the radiation in a crystal, and it manifests itself much more weakly in the amorphous case. When the observation angles tend to 180°, the incoherent cross-section falls rapidly. Contribution of the interference term to the total cross-section depends on the charge sign of the projectile. By this reason, the angular behaviour of the cross-section near the small observation angles will be opposite in the case of a relativistic positron. For comparison, the polarization cross-section for the case of a silicon amorphous target is shown in fig. 8 by the solid line. Angular dependence of this cross-section is similar to that which was obtained in [18] using the local electron density method and the Thomas-Fermi statistical model. It achieves maximal val-

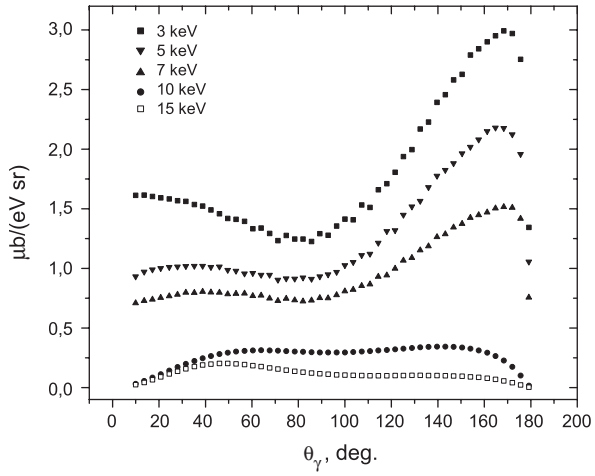

Fig. 9. The polarization three-folded cross-section in a silicon crystal as a function of θ_γ for some selected photon energies.

ues near the forward direction, has the minimum at angles about 90° and then increases slowly at $\theta_\gamma > 90°$.

Note, that we did not take into account the nuclear-structure effects, which were studied in [19]. These effects are important at large momentum transfers only.

As the photon energy increases, the decreasing of $F(q)$ leads to the disappearance of the maximum of the incoherent cross-section. This feature is illustrated by fig. 9, where the cross-section is shown for several photon energies.

4 Conclusion

The differential and integral features for the incoherent cross-section of X-radiation produced by a relativistic electron in a single crystal, were studied for a momentum transfer region where the projectile interacts with the crystal atom as a whole, and making a significant contribution to the resulting radiation yield.

It is shown that the incoherent cross-section has a pronounced structure as a function of both the final electron angles and the photon energy. In particular, a sharp dip was found in the region of small momentum transfers, which is near to the minimum kinematically allowed momentum transfer. Note that this feature of incoherent X-radiation is at variance with static bremsstrahlung, where the cross-section has a maximum in the same region ([9],[20]).

Explicit numerical calculations have demonstrated that the three-folded incoherent cross-section for photon energies up to 10 keV achieves its maximal values near the backward angles in respect to the direction of the relativistic particles.

Our findings could be useful to analyse results of experiments where coherent processes resulting from the interaction of relativistic particles with crystals (*e.g.*, coherent X-radiation, channeling radiation, as well as interference effects between them) are studied.

This work was partially supported by CNPq and FAPESP.

References

1. J. Freudenberger *et al.*, Phys. Rev. Lett. **74**, 2487 (1994).
2. D.I. Adejishvili *et al.*, Nucl. Instrum. Methods Phys. Res. B **152**, 406 (1999). It should be noted that in eq. (1) of this reference the term in square brackets must be squared.
3. D.I. Adejshvili *et al.*, *Line width of parametric X-radiation type B measured in germanium at electron energy 25.4 MeV*, preprint KFTI 95-10, Kharkov (1995).
4. V.B. Gavrikov *et al.*, Braz. J. Phys. **29**, 516 (1999).
5. S.V. Blazhevich *et al.*, Phys. Lett. A **195**, 210 (1994).
6. V.B. Gavrikov *et al.*, Nucl. Instrum. Methods Phys. Res. A **457**, 411 (2001).
7. M.L. Ter Mikaelyan, Zh. Eksp. Teor. Fiz. **25**, 296 (1953).
8. H. Uberall, Phys. Rev. **103**, 1055 (1956).
9. L.C. Maximon *et al.*, Phys. Rep. **147**, 4 (1987).
10. J. Freudenberger *et al.*, Phys. Rev. Lett. **84**, 270 (2000).
11. M.Ya. Amusia, Phys. Rep. **162**, 5; 249 (1988).
12. V.N. Tsytovich, I.M. Oiringel (Editors), *Polarization Bremsstrahlung* (Plenum Publ., New York-London, 1992).
13. W. Heitler, *The Quantum Theory of Radiation* (Clarendon Press, Oxford, 1954).
14. M.Ya. Amusia *et al.*, Sov. Phys. JETP **61**, 224 (1985).
15. V.B. Gavrikov, Ph.D. thesis, Kharkov State University, Kharkov, 1996, available from the author upon request.
16. M.N. Martins *et al.*, Nucl. Instrum. Methods Phys. Res. A **390**, 375 (1997).
17. J.H. Hubbell *et al.*, J. Phys. Chem. Ref. Data **4**, 471 (1975).
18. V.A. Astapenko *et al.*, Sov. Phys. JETP **90**, 5; 788 (2000).
19. D.F. Hubbard, M.E. Rose, Nucl. Phys. **84**, 3; 337 (1966).
20. V.P. Likhachev *et al.*, Nucl. Instrum. Methods Phys. Res. A **457**, 415 (2001).